Research Article

Thippani Thirupathi and Kothandaraman Ramanujam*

Carbon supported g-C_3N_4 for electrochemical sensing of hydrazine

https://doi.org/10.1515/eetech-2018-0003
Received Aug 28, 2017; accepted Mar 31, 2018

Abstract: This study reports a synthesis of carbon supported graphitic carbon nitride (g-C_3N_4-KBC) obtained by pyrolysis of melamine with Ketjenblack 600JD carbon (KBC) at 550°C for 4 h in a N_2 atmosphere. g-C_3N_4-KBC oxidizes hydrazine at an onset potential 0.145 V *vs.* SCE close to the thermodynamic standard potential of hydrazine (0.23 V *vs.* SHE). In comparison to the controls, KBC and g-C_3N_4, g-C_3N_4-KBC oxidizes hydrazine at lower overpotential. Most research has tended to focus on transition metal-based catalysts and few are of carbon material such as graphene nanoflakes, graphene oxide, and carbon nanotubes. A comparison in terms of sensitivity, detection range and stability reveals g-C_3N_4-KBC electrode's superiority over other carbon material-based catalysts. To the best of our knowledge, the g-C_3N_4-KBC catalyst is not reported for sensing hydrazine in the literature.

Keywords: g-C_3N_4-KBC, hydrazine sensing, overpotential, electrochemical sensor

1 Introduction

Recently graphitic carbon nitride (g-C_3N_4) is in the spotlight owing to its applications in photo-degradation [1], photocatalytic hydrogen generation [2], oxygen reduction reaction [3], conversion of benzene to phenol [4], carbon dioxide sequestration [4] etc. g-C_3N_4 is a semiconductor and most stable allotrope at ambient condition [1]. Moreover, as g-C_3N_4 is made with strong covalent bonds between carbon and nitrogen, it is stable under light irradiation (for photocatalytic application), as well as in acidic and basic solution (for electrocatalysis applications such as ORR and CO_2 sequestration). This high stability coupled with moderate band gap makes g-C_3N_4 a suitable material for photocatalytic works. Many precursors, such as dicyandiamide, cyanamide, and melamine have been employed to synthesize g-C_3N_4. The former two precursors are expensive and hazardous in comparison to melamine. Several researchers synthesized g-C_3N_4 by heat-treatment of melamine in low-vacuum systems [5, 6]. Reaction conditions decide the extent of condensation and hence the resultant properties.

World health organization (WHO) has identified hydrazine (N_2H_4) as a group B2 human carcinogen [7]. Hence, it is vital to develop cost effective and fast sensing sensors for N_2H_4 detection. Hydrazine is a known neurotoxin, carcinogenic, mutagenic and hepatotoxic substance that harms the liver and brain glutathione. It is heavily employed in rocket fuels, weapons of mass destruction, missile and fuel cell systems [8, 9]. Further, in industries, hydrazine is used as a corrosion inhibitor, oxygen scavenger, emulsifier and antioxidant [10]. Myriad techniques are known for detecting N_2H_4 including colorimetry [11], conductometry [12], fluorescence [13] and electrochemical [14]. Among these methods, the electrochemical method offers several benefits in terms of sensitivity, selectivity, low detection limit, wide linear range, and stability. Electrochemical oxidation of N_2H_4 is limited by kinetically sluggish N_2H_4 oxidation reaction and high overpotential involved in the reaction. A plethora of noble metal-based materials has been reported to reduce the overpotential of N_2H_4 sensing [15–25]. But, only few metal-free catalysts are known for N_2H_4 sensing, they are based on either carbon nanoflakes or graphene oxide or carbon nanotubes.

This paper proposes a new material (g-C_3N_4-KBC) for electrochemical sensing of N_2H_4. g-C_3N_4-KBC is obtained by pyrolysis of melamine with carbon at 550 °C. The vital function of carbon is to impart electrical conductivity in the g-C_3N_4-KBC catalyst as g-C_3N_4 is semiconducting in nature.

***Corresponding Author: Kothandaraman Ramanujam:** Department of Chemistry, IIT Madras, Chennai 600 036, India;
Email: rkraman@iitm.ac.in, Fax: 91-44-2257 4202
Thippani Thirupathi: Department of Chemistry, IIT Madras, Chennai 600 036, India

2 Experimental

2.1 Materials

Melamine and 5 wt.% Nafion 117 ionomer solution were procured from Alfa Aesar (Kolkata, India). Ketjenblack 600JD (KBC) was obtained from Akzo Nobel (Chicago, IL). Na_2HPO_4 and NaH_2PO_4 were procured from Thermo Fisher Scientific and Loba Chemie Pvt. Ltd. Mumbai, respectively. Hydrazine was procured from Qualigens Fine Chemicals, Mumbai, India. All the solutions were prepared using Milli Q water (18 MΩ cm resistivity).

2.2 Preparation of carbon supported g-C_3N_4 (g-C_3N_4-KBC)

g-C_3N_4-KBC was prepared by one step pyrolysis process. 200 mg of melamine was dispersed in 50 mL of isopropyl alcohol, followed by addition of 100 mg of KBC. The dispersion was stirred using magnetic stirrer overnight followed by heating at 95°C to obtain well-mixed melamine-carbon composite. Thus obtained melamine-carbon composite was pyrolyzed at 550°C for 4 h in the N_2 atmosphere to obtain g-C_3N_4-KBC. g-C_3N_4 obtained by pyrolysis of the neat melamine at 550°C for 4 h was used as a reference compound in this study.

2.3 Preparation of g-C_3N_4-KBC modified glassy carbon electrode (g-C_3N_4-KBC/GCE)

Glassy carbon electrode (GCE) was polished with alumina powder (0.05 µM) followed by sonication in isopropyl alcohol and Milli Q water for 5 minutes. 5 mg of the g-C_3N_4-KBC was dispersed by sonication in 1600 µL of water-isopropyl alcohol (5:1 V/V) solution to obtain an ink-like dispersion. 12.5 µL of 5 wt.% Nafion ionomer solution was added to the ink to act as a binder. The required amount of this ink was drop-cast onto GCE and let dry in ambient conditions for 1 h to obtain a catalyst loading of 200 µg cm^{-2}.

2.4 Electrochemical evaluation

All the electrochemical measurements were performed using a Biologic VSP-300 model potentiostat and a three electrode setup. Saturated calomel electrode (SCE), Pt-mesh and catalyst coated GC electrode were used as the reference, counter and working electrodes respectively. All the electrochemical experiments were performed at 25°C in 0.1 M phosphate buffer solution (PBS, pH 7.0) electrolyte. Cyclic voltammetry (CV) was performed in the voltage range of −0.25 to 0.55 V *vs.* SCE. 5 mM ferrocyanide/ferricyanide redox couple dissolved in 0.1 M KNO_3 was used as the electrolyte. Amperometric experiments were carried out using catalyst coated glassy carbon rotating disc electrode (RDE, 5 mm glassy carbon, Pine instruments) rotating at 200 rpm and held at 0.35 V *vs.* SCE in PBS solution with a successive addition of hydrazine to the buffer solution. Electrochemical impedance spectroscopy (EIS) measurements of the electrodes were carried out in 5 mM ferrocyanide/ferricyanide dissolved in 0.1 M KNO_3 solution. A voltage perturbation (ΔV_{rms}) of 10 mV was used for impedance measurement in the frequency range of 200 kHz to 100 mHz.

2.5 Characterization techniques

The catalyst samples were characterized using powder X-ray diffraction (XRD, Bruker 8 fitted with Cu K_α X-ray source) at a scan rate of 1° per minute. High-resolution transmission electron microscopy (HR-TEM) characterization was carried out using JEOL JEM 2100. Raman spectroscopy was carried out using Bruker FT-Multi Ram fitted with Nd: YAG laser source (1064 nm, 1000 mW intensity). Carbon-Hydrogen-Nitrogen (CHN) analysis was performed using Perkin-Elmer 2400 series equipment. FT-IR spectroscopy study was performed using JASCO-400 Type-A equipment. Laser desorption ionization Fourier-transform ion-cyclotron-resonance mass spectrometry (LDI-FT-ICR-MS obtained from MS Solarix-JA, Brucker Daltonics) is employed to study the low-molecular-weight species existing in g-C_3N_4-KBC. X-ray photoelectron spectroscopy (XPS) of the samples was recorded using Fisons Instruments (S-ProbeTM2803) fitted with Al K_α X-ray source. The analyzer was set at a pass energy of 20 eV to obtain N 1s and C 1s spectra. Shirley-type background correction was employed to the spectra and the peaks were deconvoluted to identify the chemical states of N and C in the samples. The measured binding energies were calibrated employing the C 1s peak at 284.8 eV as the reference.

3 Results and discussion

3.1 XRD and CHN studies

XRD patterns of KBC, g-C_3N_4, and g-C_3N_4-KBC were recorded (Figure 1). KBC shows two broad peaks centered at around 26.5° (2θ) and 43.34°, that correspond to (002) and (101) planes of graphite. g-C_3N_4 shows peaks at (2θ) 13.02° and 27.68° corresponding to (100) and (002) planes, respectively [26]. In the case of g-C_3N_4-KBC, since the (002) peak from KBC is merged with the (002) peak of g-C_3N_4, the peak position could not be ascertained clearly. However, the (100) peak at 13.5° confirms the presence of g-C_3N_4. CHN analysis of g-C_3N_4 and g-C_3N_4-KBC indicates C:N ratio of 36:63 (remaining 1 % is from H) and 67:32, respectively. As the C:N ratio of g-C_3N_4 is closer to the theoretical C:N ratio of 34:66, the formation of g-C_3N_4 from pyrolysis of melamine is confirmed.

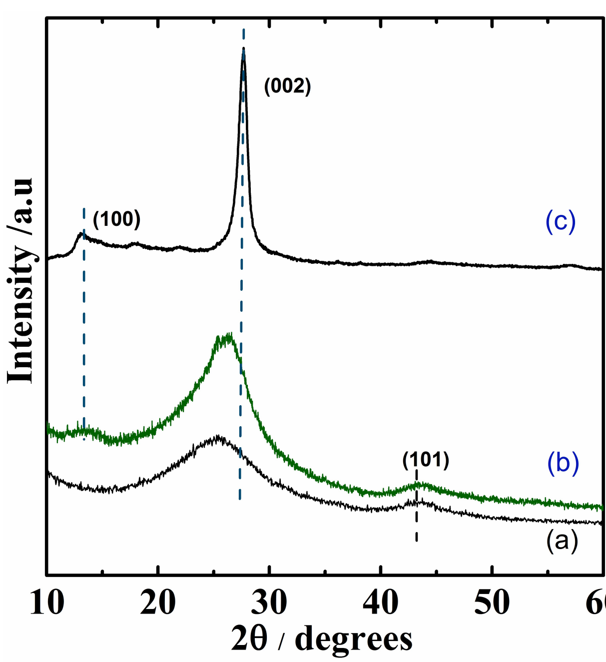

Figure 1: X-ray diffraction patterns of (a) KBC, (b) g-C_3N_4-KBC, and (c) g-C_3N_4.

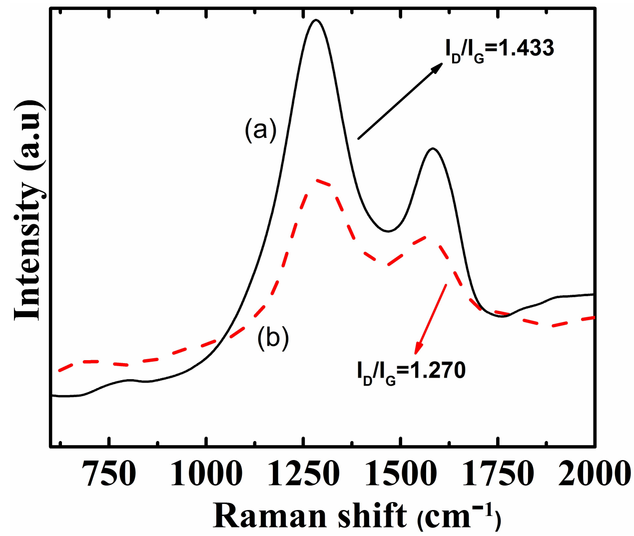

Figure 2: Raman spectra of (a) KBC and (b) g-C_3N_4-KBC.

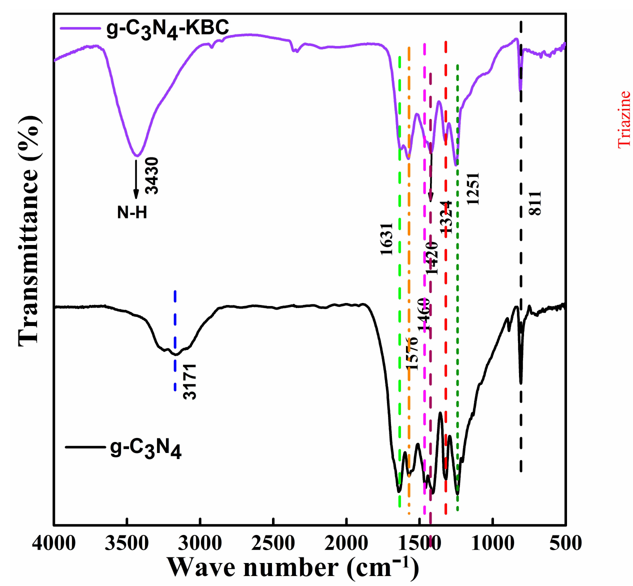

Figure 3: FT-IR-spectra of g-C_3N_4 and g-C_3N_4-KBC.

3.2 Raman and FT-IR spectroscopy studies

Raman spectra of g-C_3N_4-KBC and KBC are shown in Figure 2. I_D/I_G ratio of KBC and g-C_3N_4-KBC are about 1.43 and 1.27, respectively. As the carbons of g-C_3N_4 are sp^2 hybridized, the composite g-C_3N_4-KBC has more intensity for G-band over D-band and hence the I_D/I_Gratio of g-C_3N_4-KBC is smaller than that of the KBC. FT-IR spectra (Figure 3) of both g-C_3N_4 and g-C_3N_4-KBC feature peaks due to C=N (1631 cm^{-1}), C-N (1251, 1324, 1420, 1460 and 1576 cm^{-1}) stretching and out of plane breathing mode of triazine ring (811 cm^{-1}). For g-C_3N_4-KBC, N-H stretching is observed [27] at around 3430 cm^{-1}. In the case of g-C_3N_4, there was no peak at around 3430 cm^{-1}, however, there was a broad peak at 3171 cm^{-1} due to hydrogen-bonding interactions [28]. The absence of strong H-bonding interactions on g-C_3N_4-KBC probably due to the concentration of g-C_3N_4 on KBC is lower than that of the neat g-C_3N_4 limiting the H-bonding interactions among the -NH_2 func-

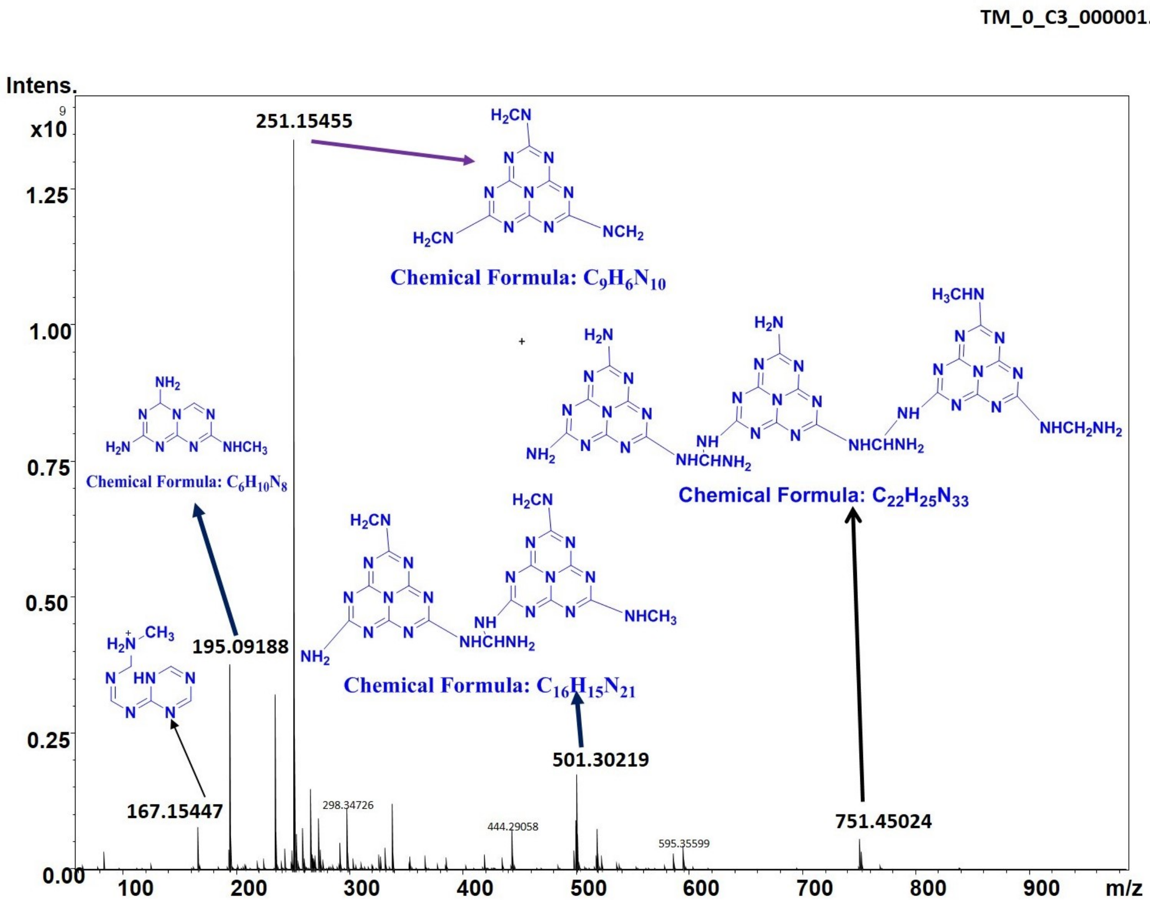

Figure 4: LDI-FT-ICR-MS spectrum of g-C_3N_4-KBC.

tional groups of g-C_3N_4 particles. It is to be noted that CHN analysis indicated the presence of 1 wt.% of H in neat g-C_3N_4, whereas the H content was below detection limit in g-C_3N_4-KBC.

3.3 LDI-FT-ICR-MS

Figure 4 shows the LDI-FT-ICR-MS of g-C_3N_4-KBC with the structure of the possible species. The most intense peak at m/z 251.15 is the base peak. The peak at m/z of 751 is a molecular ion peak due to $C_{22}H_{25}N_{33}$, which contains three heptazine ring moieties (2D-network of heptazine) [29]. The peaks below m/z of 751 are labeled with the possible decomposition products of $C_{22}H_{25}N_{33}$.

3.4 XPS and TEM studies

XPS measurement was conducted to probe the elemental chemical spectra and the N/C atomic ratio in g-C_3N_4-KBC. The survey spectrum shows the presence of C, N, and O (Figure 5(a)). Figure 5(b) shows the high-resolution C 1s spectrum, wherein presence of C=C (284.6 eV), C=O/C-N (285.6 eV), C=N (288 eV) and O-C=O (290.3 eV) functional groups were identified by deconvoluting the peaks [30]. The peak C-N originates from g-C_3N_4. Deconvolution of N 1s spectra (Figure 5(c)) indicates presence of C=N-C (398.7 eV), N-$(C)_3$ (399.6 eV) and pyridinic-oxide (404.7 eV) [30]. XPS measured N/C atomic ratio is 3.9, which is close to that of the theoretical N-C ratio of g-C_3N_4 confirming the formation of g-C_3N_4 on KBC surface during pyrolysis. HR-TEM image of the g-C_3N_4-KBC shows the presence of ordered region, which are possibly due to the layers of g-C_3N_4 (Figure 6).

4 Electrochemical studies

4.1 Cyclic voltammetric studies

Electrokinetic parameters of the KBC and g-C_3N_4-KBC were analyzed using CV performed in potassium ferro/ferri

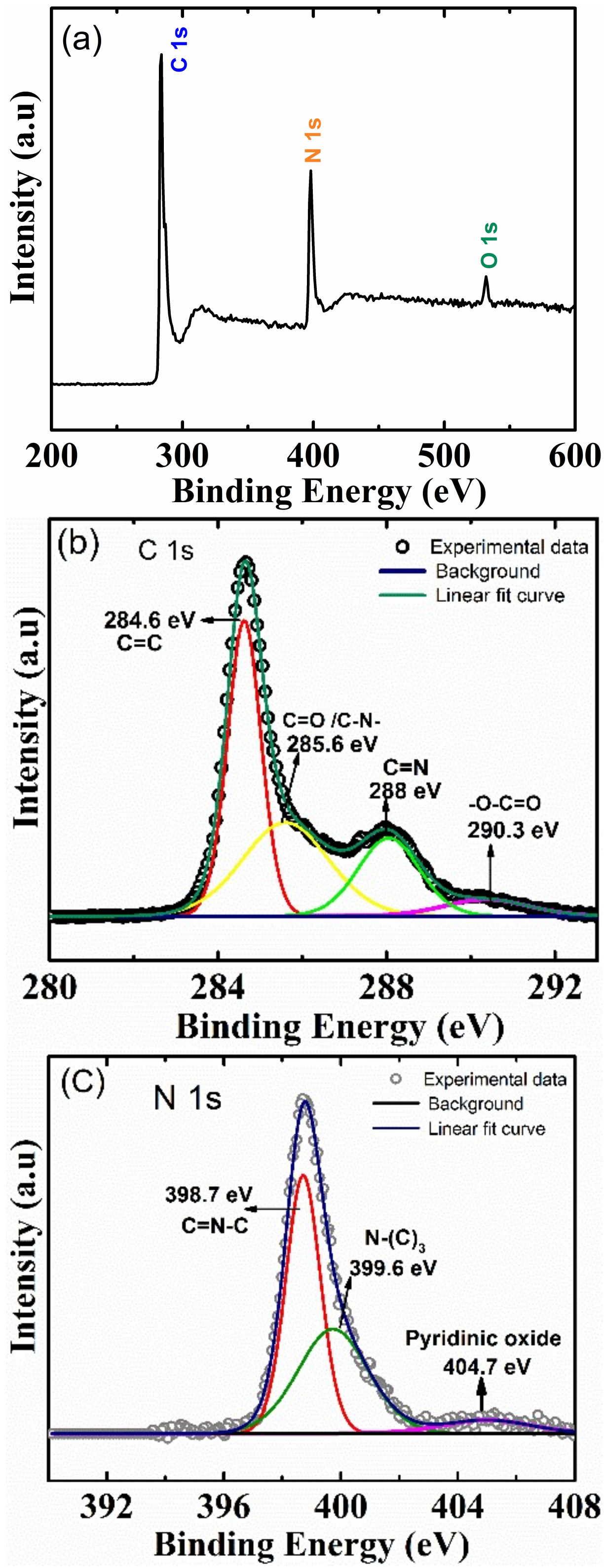

Figure 5: (a) Survey scan and high resolution, (b) C 1s, and (c) N 1s spectra of g-C_3N_4-KBC.

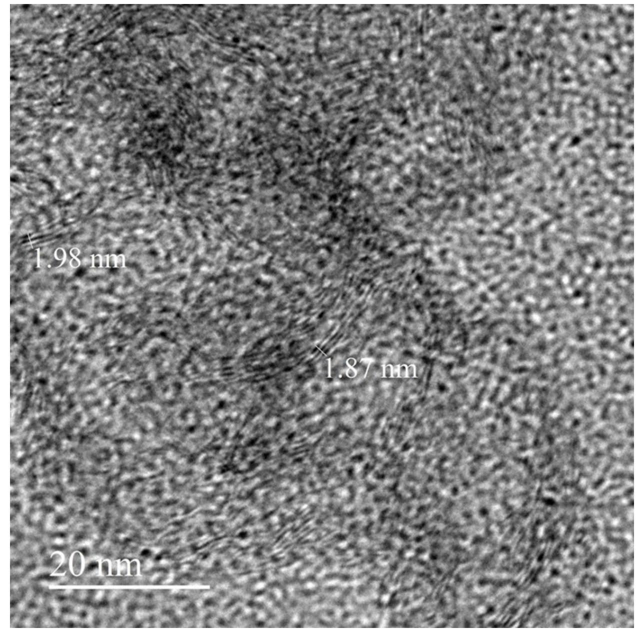

Figure 6: TEM micrograph of g-C_3N_4-KBC.

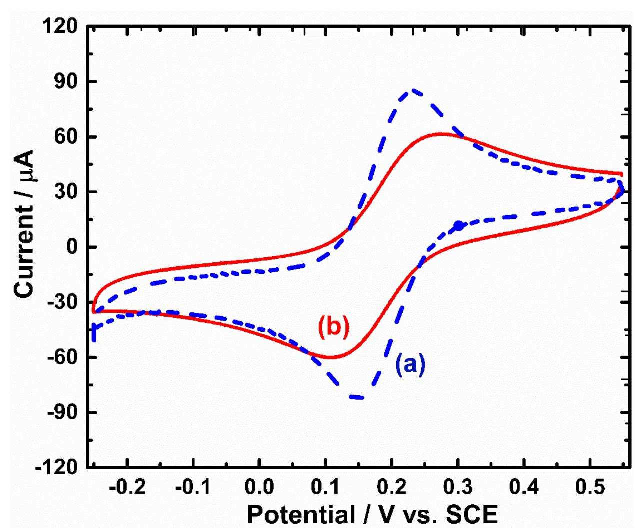

Figure 7: Cyclic voltammogram of (a) g-C_3N_4-KBC and (b) KBC electrodes recorded at 20 mV s^{-1} scan rate at 25°C in a solution containing 5 mM of each potassium ferricyanide and potassium ferrocyanide in 0.1M potassium nitrate solution.

cyanide containing electrolyte. In the CV, g-C_3N_4-KBC shows higher redox current values and lower peak-to-peak potential separation (ΔE_p) in comparison to that of the KBC. ΔE_p value of g-C_3N_4-KBC is 79 mV, which indicates the close to Nernstian behavior (~59 mV) of the ferro/ferricyanide redox couple on the g-C_3N_4-KBC electrode surface. ΔE_p of KBC is around 137 mV indicating quasi-redox behavior of ferro/ferri cyanide. Further, heterogeneous electron transfer rate constant (k_s) values

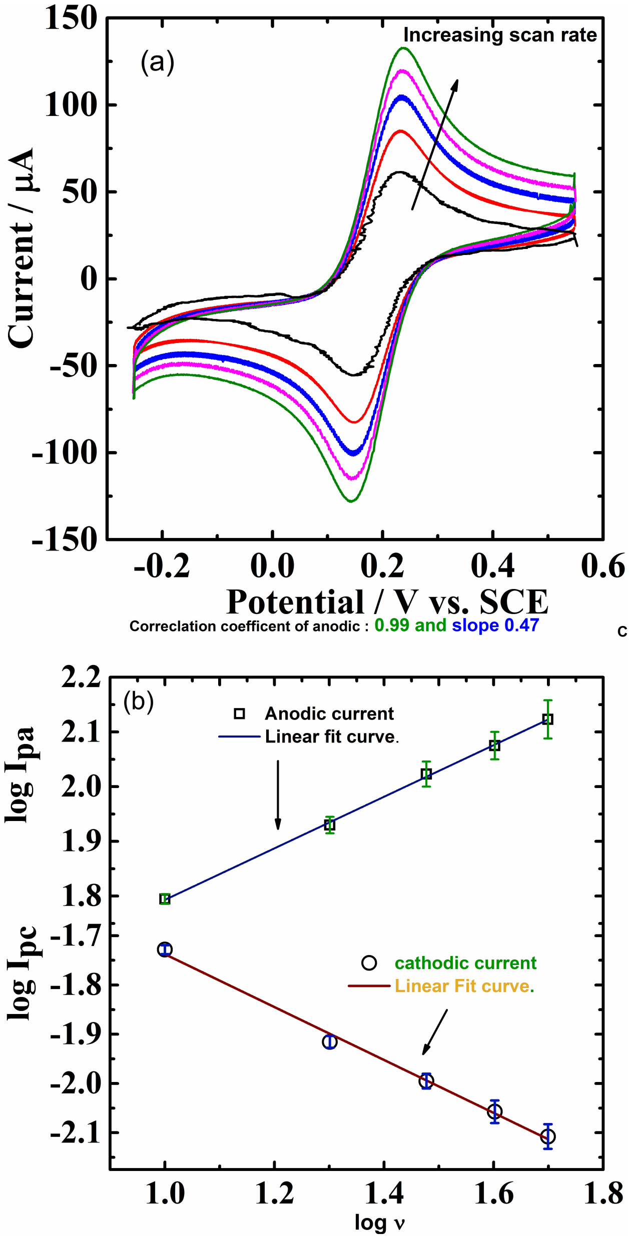

Figure 8: (a) Cyclic voltammograms of g-C_3N_4-KBC recorded at different scan rates (10-50mV s^{-1}) at 25°C in a solution containing 5 mM of each potassium ferricyanide and potassium ferrocyanide in 0.1M potassium nitrate solution and (b) log Ip Vs. log v plot derived from the CVs recorded at different scan rates.

were calculated for g-C_3N_4-KBC and KBC using Laviron equation (eq. 1). k_s value of g-C_3N_4-KBC and KBC are 0.3 s^{-1} and 0.24 s^{-1}, respectively. Muthyal *et al.* [31] have reported a k_s value of 0.4 s^{-1} for graphene nanoflakes. Potassium ferro/ferricyanide redox reaction is an outer-sphere electron transfer reaction. Hence, high k_s value indicates good electrical conductivity of the electrode surface. As g-C_3N_4 is a semiconductor, if it is not uniformly supported by KBC, a low k_s value is expected. Since the k_s value of g-C_3N_4-KBC is close to that of KBC, we surmise that g-C_3N_4-KBC to remain as conducting as KBC.

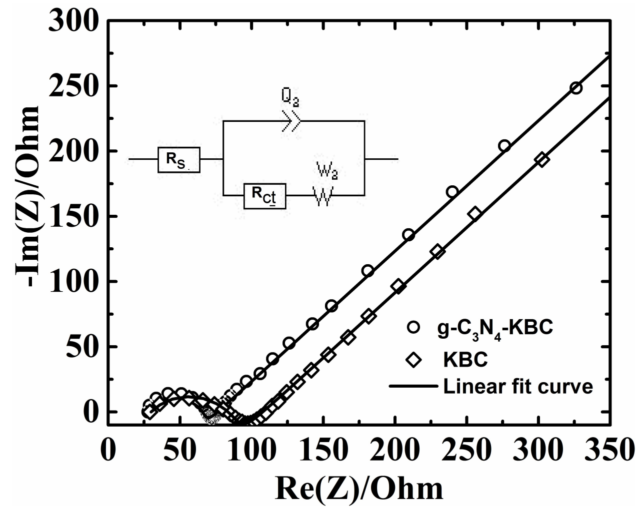

Figure 9: Electrochemical impedance spectroscopy (EIS) responses of KBC and g-C_3N_4-KBC solution containing 5 mM of potassium ferricyanide and potassium ferrocyanide in 0.1 M KNO_3 solution.

$$\log k_s = \alpha log(1-\alpha) + (1-\alpha)\log\alpha - \log\frac{RT}{nFv} - \frac{\alpha(1-\alpha)nF\Delta E_p}{2.303\,RT} \quad (1)$$

Where n is the number of electrons involved in electrochemical reaction, F is the Faraday constant (96486 C mol^{-1}); k_s is the heterogeneous electron transfer rate constant (s^{-1}); R is the gas constant (8.314 J K^{-1} mol^{-1}); v is the scan rate (V s^{-1}); T is the absolute temperature and $\alpha$is the transfer coefficient (0.5).

Figure 8(a) shows the CVs of g-C_3N_4-KBC recorded at different scan rates from 10 mV s^{-1} to 50 mV s^{-1}. The anodic and cathodic peak currents of g-C_3N_4-KBC electrode increase with increase in scan rate (v) *i.e.* follow the Randles-Sevcik equation. In both cases, the obtained correlation coefficient is 0.99, which indicates that g-C_3N_4-KBC has unique electronic structure with fast electrode kinetics [32]. A plot of log i vs. log v (Figure 8(b)) displays a linear behavior and portrays a gradient of 0.47, which confirms that electroactive behavior of ferro/ferri cyanide at g-C_3N_4-KBC electrode is a diffusion controlled process [33].

4.2 Electrochemical impedance spectroscopy

Further, the electron transfer characteristics of g-C_3N_4-KBC modified GC electrode and KBC were characterized by EIS at open circuit potential in ferro/ferricyanide containing electrolyte. Figure 9 shows the Nyquist plot, where a semicircle followed by a linear portion is observed. The semicircle corresponds to charge transfer process, and the linear portion at lower frequencies corresponds to diffusion process. The equivalent circuit used for fitting the experimental EIS data is shown as inset in Figure 9. The charge transfer resistance (R_{ct}) of the ferro/ferricyanide redox couple at the electrode surface is quantified from the diameter of the semicircle. R_{ct} values of 44 Ω and 68 Ω are observed for g-C_3N_4-KBC and KBC electrodes, respectively. The lower R_{ct} value of g-C_3N_4-KBC indicates its higher electrocatalytic activity towards ferro/ferricyanide in comparison to that of KBC. Table 1 lists the EIS parameters Q, R_{ct} and n*.

Table 1: List of the EIS parameters of KBC and g-C_3N_4-KBC electrodes measured at open circuit potentials.

Electrode name	Charge transfer resistance (R_{ct}) / Ohm	Constant-phase-element (Q) / F·s$^{(n-1)}$	n*
KBC	68 ± 2.2	0.264 (8) × 10^{-6}	0.6
g-C_3N_4-KBC	44 ± 0.7	0.141 (2) ×10^{-6}	0.5

Where n* = Constant phase element ideality factor associated with the distortion of the capacitance due to electrode surface roughness

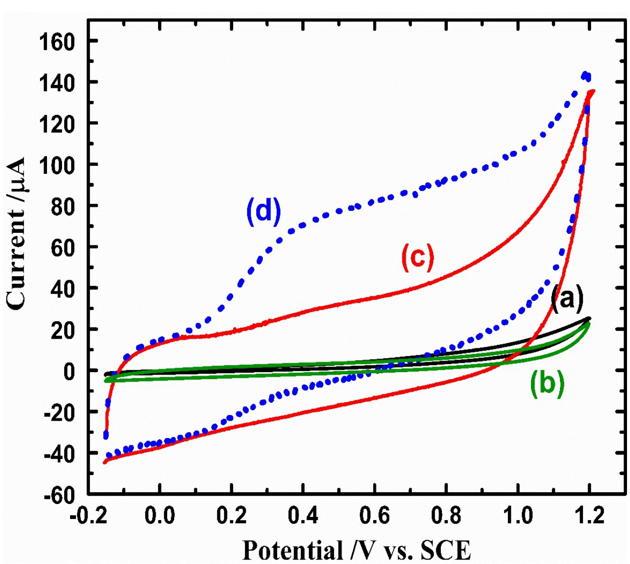

Figure 10: Cyclic voltammograms of (a) GCE, (b) g-C_3N_4, (c) KBC, and (d) g-C_3N_4-KBC electrodes in 1 mM N_2H_4 containing PBS (pH= 7.0) measured at scan rate 0.05 V s^{-1} scan rate.

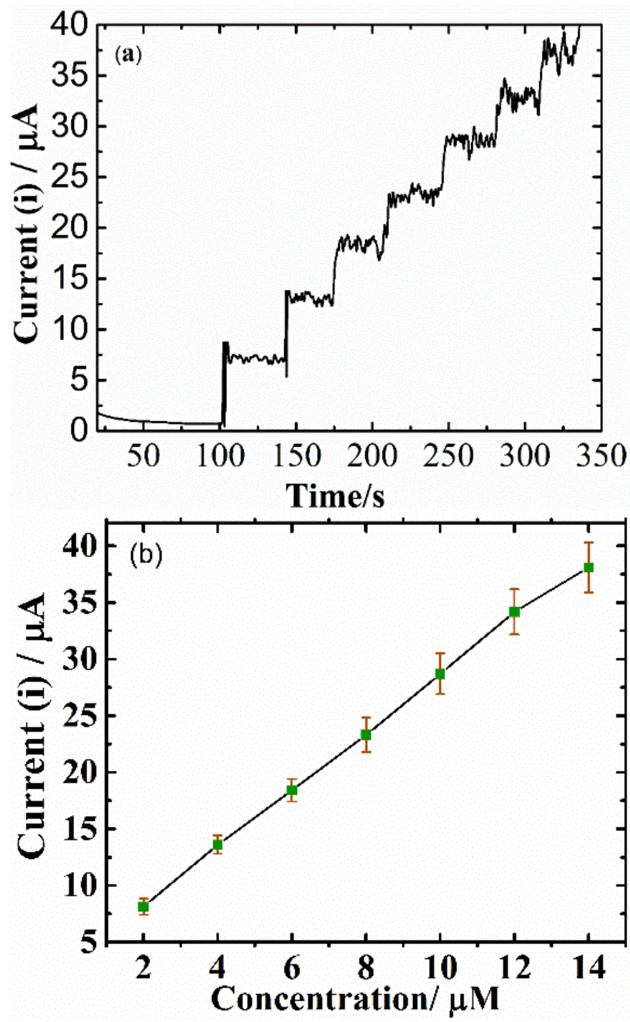

Figure 11: (a) Amperometric response of g-C_3N_4-KBC electrode in PBS (pH 7.0) for successive addition of 2 µM of hydrazine and (b) the corresponding calibration plot of Figure 11(a) obtained using three freshly prepared g-C_3N_4-KBC electrodes.

4.3 Electrochemical oxidation of N_2H_4

A hydrazine electrochemical sensor was set up using g-C_3N_4-KBC as electrode material. Figure 10 compares the CV profiles of g-C_3N_4-KBC, KBC, g-C_3N_4, and GCE in 1 mM hydrazine containing PBS solution. g-C_3N_4-KBC showed very low onset potential of about 0.145 V vs. SCE in comparison to that of the KBC, GCE, and g-C_3N_4. Due to low surface area of the GCE, the double layer current observed in the potential region −0.2 to 1.2 V is lowest for GCE. Similarly, due to the semiconducting nature of g-C_3N_4, the double layer current is very low for g-C_3N_4/GCE as well. g-C_3N_4-KBC has both electrical conductivity and catalytic activity towards N_2H_4, hence showed lower overpotential towards N_2H_4 oxidation and higher double layer current,

Table 2: Comparison of E_{onse}t, sensitivity, linear range, and detection limit of different electrode materials towards N_2H_4 sensing at pH7

Electrode	E_{onset} / V *vs.* SHE	Sensitivity / μA/mM	Linear Range / μM	Limit of detection (LOD) / μM	Reference
MSS-Co(salen)/GCE	0.360	-	10-210	-	[34]
Cus/rGO/GCE	0.326	7.96	1-1000	0.3	[35]
MSS-Co(salophen)/GCE	0.090	-	10-50	-	[34]
NPC-2 / GCE	0.200	45.2	1-330	0.47	[22]
WO_3 NPs/Au modified electrode	0.222	0.005	100-1000	144.73	[36]
GCE / Au-MSM	0.206	1.62	500-18000	0.11	[37]
$(PANI/Au_0)_5$/GCE	0.177	-	10-6000	1	[38]
AuNP-GPE	0.197	-	0.05-25	3.07	[39]
PdHCF-Al	0.872	-	390-10,000	4.6	[40]
GNF/GCE	0.347	0.028	0.5-7.5	0.3	[31]
$NiFe_2O_4$/MWCNTs/GC	0.431	-	5-2500	1.5	[41]
RMWCNT/GCE	0.160	0.065	2-190	0.61	[42]
BiHCF/CC	0.130	-	7-1010	3	[43]
Mn(II)-complex/MWNTs/GCE	0.225	0.038	1-1050	0.5	[44]
Manganese hexacyanoferrate	0.210	0.047	33-8, 180,000	6.65	[45]
Catechin GCE	0.110	0.008	2-58	0.16	[46]
Pd-GG-g-PAM-silica/GCE	0.151	33.26	600-180,000	4.1	[47]
HMWCNT/GCE	0.125	0.020	2-122	0.68	[48]
Graphene/GCE	0.206	-	3 -300	1.0	[49]
RGO/GCE	0.550	-	-	-	[50]
PDA-RGO/GCE	0.430	-	0.03-100	0.01	[50]
g-C_3N_4-KBC	0.386	2.5	2-14	0.7	This work

which is nearly similar to that of KBC in the potential region −0.2 to 0 V.

In comparison to GCE, the current due to hydrazine oxidation observed on KBC was higher due to high surface area of KBC (~1400 m^2/g). The thermodynamic standard potential of hydrazine oxidation is 0.23 V.

$$N_2H_5^+ \rightarrow N_{2(g)} + 5H^+ + 4e^- \quad (2)$$
$$E^0 = 0.23\ V\ Vs.\ SHE$$

g-C_3N_4-KBC oxidizes N_2H_4 at an onset potential close to that of E^0 of N_2H_4. Similar onset potential is reported for hydrazine oxidation on graphene nanoflakes [17]. Eq. 3 shows the overall mechanism involved in N_2H_4 oxidation

$$N_2H_{4(l)} \rightarrow N_{2(g)} + 4H^+ + 4e^- \quad (3)$$

The g-C_3N_4-KBC sensor is further characterized using chronoamperometry, to understand its detection limit, sensitivity and signal-to-noise ratio.

Figure 11 (a) portrays the steady-state response obtained for hydrazine oxidation at 0.35 V vs. SCE on g-C_3N_4-KBC electrode with successive addition of 2 μM hydrazine in PBS. A calibration plot was made (Figure 11(b)) plotting the steady-state current against the concentration of the N_2H_4. This plot shows a good linear fit in the concentration range of 2 μM to 14 μM with a correlation coefficient of 0.99. The sensitivity and limit of detection were 2.5 μA/μM and 0.7 μM respectively, with a signal-to-noise (S/N) ratio of 3. In the literature, most of the hydrazine sensors reported are based on transition metal-based catalysts. There are few reports using carbon materials such as graphene nanoflakes, graphene oxide, and carbon nanotubes. Table 2 compares the sensitivity, linear range, and limit of detection of various materials reported in the literature.

Selectivity plays a vital role in sensor characterization. Real samples contain many species along with N_2H_4 which could probably respond in the same potential region as N_2H_4. Most common interferences are H_2O_2, uric acid, glucose, Cu^{2+}, Ca^{2+}, K^+, and Na^+. Although Cu^{2+}, Ca^{2+}, K^+, and Na^+ cannot be oxidized further, they may interfere in the kinetics of the hydrazine oxidation on g-C_3N_4-KBC (Figure 12). 20 μM hydrazine was used in this study and 3-times more of glucose, uric acid and H_2O_2 were injected and found not to interfere with N_2H_4 sensing. Similarly, Cu^{2+}, Ca^{2+}, K^+, and Na^+ are injected at 60 μM concentration and found not to interfere with N_2H_4 sensing. This experiment demonstrated the high selectivity towards N_2H_4 sensing on g-C_3N_4-KBC.

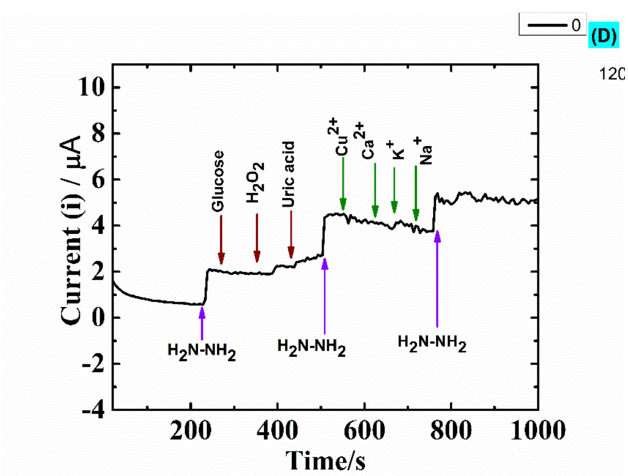

Figure 12: Amperometric response of g-C_3N_4-KBC in a PBS solution containing 20 μM N_2H_4 and three-fold concentration of different interfering species hydrogen peroxide, uric acid, Na^+, Ca^{2+}, Cu^{2+}, K^+, and glucose.

5 Conclusions

Pyrolysis of melamine leads to formation of g-C_3N_4. Formation of g-C_3N_4 was confirmed using XRD, FT-IR, CHN, XPS, LDI-FT-ICR-MS and TEM studies. This work demonstrates the N_2H_4 sensing property of g-C_3N_4-KBC. It oxidizes N_2H_4 at an onset potential closer to that of the thermodynamic oxidation potential of N_2H_4. Using chronoamperometry, the detection limit, linear range, sensitivity, and signal-to-noise ratio were measured. g-C_3N_4-KBC exhibited a detection limit of 0.7 μM with a sensitivity of 2.5 μA/μM. In this study, the amperometric response of the interfering electroactive species such as Ca^{2+}, Cu^{2+}, K^+, Na^+, glucose, uric acid, and H_2O_2 were examined and found not to interfere with N_2H_4 sensing.

Acknowledgement: We thank DST-New Delhi for financial support (DST (SB/FT/CS-171/2013). Thippani Thirupathi thanks the UGC-CSIR for fellowship.

References

[1] Yan SC, Li ZS, Zou ZG (2009) Photodegradation performance of g-C_3N_4 fabricated by directly heating melamine. Langmuir 25:10397–10401.
[2] Teets TS, Nocera DG (2011) Photocatalytic hydrogen production. Chem Commun 47:9268–9274.
[3] Zheng Y, Jiao Y, Chen J, et al. (2011) Nanoporous graphitic-C_3N_4@ carbon metal-free electrocatalysts for highly efficient oxygen reduction. J Am Chem Soc 133:20116–20119.
[4] Chen X, Zhang J, Fu X, et al. (2009) Fe-g-C_3N_4-catalyzed oxidation of benzene to phenol using hydrogen peroxide and visible light. J Am Chem Soc 131:11658–11659.
[5] Komatsu T (2001) Attempted chemical synthesis of graphite-like carbon nitride. J Mater Chem 11:799–801.
[6] Zhao YC, Yu DL, Yanagisawa O, et al. (2005) Structural evolution of turbostratic carbon nitride after being treated with a pulse discharge. Diam Relat Mater 14:1700–1704.
[7] Rastakhiz N, Kariminik A, Soltani-Nejad V, Roodsaz S (2010) Simultaneous determination of phenylhydrazine, hydrazine and sulfite using a modified carbon nanotube paste electrode. Int J Electrochem Sci 5:1203–1212.
[8] Ensafi AA, Mirmomtaz E (2005) Electrocatalytic oxidation of hydrazine with pyrogallol red as a mediator on glassy carbon electrode. J Electroanal Chem 583:176–183.
[9] Zelnick SD, Mattie DR, Stepaniak PC (2003) Occupational exposure to hydrazines: treatment of acute central nervous system toxicity. Aviat Space Environ Med 74:1285–1291.
[10] Garrod S, Bollard ME, Nicholls AW, et al. (2005) Integrated metabonomic analysis of the multiorgan effects of hydrazine toxicity in the rat. Chem Res Toxicol 18:115–122.
[11] Sun M, Guo J, Yang Q, et al. (2014) A new fluorescent and colorimetric sensor for hydrazine and its application in biological systems. J Mater Chem B 2:1846–1851.
[12] Kumar S, Bhanjana G, Dilbaghi N, Umar A (2015) Zinc oxide nanocones as potential scaffold for the fabrication of ultra-high sensitive hydrazine chemical sensor. Ceram Int 41:3101–3108.
[13] Sun Y, Zhao D, Fan S, Duan L (2015) A 4-hydroxynaphthalimide-derived ratiometric fluorescent probe for hydrazine and its in vivo applications. Sensors Actuators B Chem 208:512–517.
[14] Dudin P V, Unwin PR, Macpherson J V (2011) Electro-oxidation of hydrazine at gold nanoparticle functionalised single walled carbon nanotube network ultramicroelectrodes. Phys Chem Chem Phys 13:17146–17152.

[15] Conway BE, Marincic N, Gilroy D, Rudd E (1966) Oxide involvement in some anodic oxidation reactions. J Electrochem Soc 113:1144–1158.
[16] Karp S, Meites L (1962) The Voltammetric Characteristics and Mechanism of Electroöxidation of Hydrazine. J Am Chem Soc 84:906–912.
[17] Aldous L, Compton RG (2011) Towards mixed fuels: the electrochemistry of hydrazine in the presence of methanol and formic acid. ChemPhysChem 12:1280–1287.
[18] Aldous L, Compton RG (2011) The mechanism of hydrazine electro-oxidation revealed by platinum microelectrodes: role of residual oxides. Phys Chem Chem Phys 13:5279–5287.
[19] Wang Y, Wan Y, Zhang D (2010) Reduced graphene sheets modified glassy carbon electrode for electrocatalytic oxidation of hydrazine in alkaline media. Electrochem commun 12:187–190.
[20] Zheng L, Song J (2009) Curcumin multi-wall carbon nanotubes modified glassy carbon electrode and its electrocatalytic activity towards oxidation of hydrazine. Sensors Actuators B Chem 135:650–655.
[21] Salimi A, Miranzadeh L, Hallaj R (2008) Amperometric and voltammetric detection of hydrazine using glassy carbon electrodes modified with carbon nanotubes and catechol derivatives. Talanta 75:147–156.
[22] Yan L, Bo X, Zhang Y, Guo L (2014) Facile green synthesis of nitrogen-doped porous carbon and its use for electrocatalysis towards nitrobenzene and hydrazine. Electrochim Acta 137:693–699.
[23] Liu Y, Li Y, He X (2014) In situ synthesis of ceria nanoparticles in the ordered mesoporous carbon as a novel electrochemical sensor for the determination of hydrazine. Anal Chim Acta 819:26–33.
[24] Allen MJ, Tung VC, Kaner RB (2009) Honeycomb carbon: a review of graphene. Chem Rev 110:132–145.
[25] Tang L, Wang Y, Li Y, et al. (2009) Preparation, structure, and electrochemical properties of reduced graphene sheet films. Adv Funct Mater 19:2782–2789.
[26] Yan SC, Li ZS, Zou ZG (2009) Photodegradation performance of g-C_3N_4 fabricated by directly heating melamine. Langmuir 25:10397–10401.
[27] Liu Q, Zhang J (2013) Graphene supported Co-g-C_3N_4 as a novel metal–macrocyclic electrocatalyst for the oxygen reduction reaction in fuel cells. Langmuir 29:3821–3828.
[28] Liu J, Zhang T, Wang Z, et al. (2011) Simple pyrolysis of urea into graphitic carbon nitride with recyclable adsorption and photocatalytic activity. J Mater Chem 21:14398–14401.
[29] Striegler K (2015) Modified Graphitic Carbon Nitrides for Photocatalytic Hydrogen Evolution from Water: Copolymers, Sensitizers and Nanoparticles. Springer
[30] Hou Y, Wen Z, Cui S, et al. (2013) Constructing 2D porous graphitic C_3N_4 nanosheets/nitrogen-doped graphene/layered MoS_2 ternary nanojunction with enhanced photoelectrochemical activity. Adv Mater 25:6291–6297.
[31] Mutyala S, Mathiyarasu J (2015) Preparation of graphene nanoflakes and its application for detection of hydrazine. Sensors Actuators B Chem 210:692–699.
[32] Soldano C, Mahmood A, Dujardin E (2010) Production, properties and potential of graphene. Carbon N Y 48:2127–2150.
[33] Sims MJ, Rees N V, Dickinson EJF, Compton RG (2010) Effects of thin-layer diffusion in the electrochemical detection of nicotine on basal plane pyrolytic graphite (BPPG) electrodes modified with layers of multi-walled carbon nanotubes (MWCNT-BPPG). Sensors Actuators B Chem 144:153–158.
[34] Pal M, Ganesan V (2012) Electrocatalytic activity of cobalt Schiff base complex immobilized silica materials towards oxygen reduction and hydrazine oxidation. Catal Sci Technol 2:2383–2388.
[35] Yang YJ, Li W, Wu X (2014) Copper sulfide| reduced graphene oxide nanocomposite for detection of hydrazine and hydrogen peroxide at low potential in neutral medium. Electrochim Acta 123:260–267.
[36] Shukla S, Chaudhary S, Umar A, et al. (2014) Tungsten oxide (WO_3) nanoparticles as scaffold for the fabrication of hydrazine chemical sensor. Sensors Actuators B Chem 196:231–237.
[37] Gupta R, Rastogi PK, Ganesan V, et al. (2017) Gold nanoparticles decorated mesoporous silica microspheres: A proficient electrochemical sensing scaffold for hydrazine and nitrobenzene. Sensors Actuators B Chem 239:970–978.
[38] Xin M, Lin H, Yang J, et al. (2014) Preparation of polyaniline/Au0 nanocomposites modified electrode and application for hydrazine detection. Electroanalysis 26:2216–2223.
[39] Aziz MA, Kawde A-N (2013) Gold nanoparticle-modified graphite pencil electrode for the high-sensitivity detection of hydrazine. Talanta 115:214–221.
[40] Razmi H, Azadbakht A, Sadr MH (2005) Application of a palladium hexacyanoferrate film-modified aluminum electrode to electrocatalytic oxidation of hydrazine. Anal Sci 21:1317–1323.
[41] Fang B, Feng Y, Liu M, et al. (2011) Electrocatalytic oxidation of hydrazine at a glassy carbon electrode modified with nickel ferrite and multi-walled carbon nanotubes. Microchim Acta 175:145.
[42] Zare HR, Sobhani Z, Mazloum-Ardakani M (2007) Electrochemical behavior of electrodeposited rutin film on a multi-wall carbon nanotubes modified glassy carbon electrode. Improvement of the electrochemical reversibility and its application as a hydrazine sensor. J Solid State Electrochem 11:971–979.
[43] Zheng J, Sheng Q, Li L, Shen Y (2007) Bismuth hexacyanoferrate-modified carbon ceramic electrodes prepared by electrochemical deposition and its electrocatalytic activity towards oxidation of hydrazine. J Electroanal Chem 611:155–161.
[44] Kamyabi MA, Narimani O, Monfared HH (2010) Electrocatalytic oxidation of hydrazine using glassy carbon electrode modified with carbon nanotube and terpyridine manganese (II) complex. J Electroanal Chem 644:67–73.
[45] Jayasri D, Narayanan SS (2007) Amperometric determination of hydrazine at manganese hexacyanoferrate modified graphite–wax composite electrode. J Hazard Mater 144:348–354.
[46] Zare HR, Habibirad AM (2006) Electrochemistry and electrocatalytic activity of catechin film on a glassy carbon electrode toward the oxidation of hydrazine. J Solid State Electrochem 10:348–359.
[47] Rastogi PK, Ganesan V, Krishnamoorthi S (2014) Palladium nanoparticles decorated gaur gum based hybrid material for electrocatalytic hydrazine determination. Electrochim Acta 125:593–600.
[48] Zare HR, Nasirizadeh N (2007) Hematoxylin multi-wall carbon nanotubes modified glassy carbon electrode for electrocatalytic oxidation of hydrazine. Electrochim Acta 52:4153–4160.
[49] Wang C, Zhang L, Guo Z, et al. (2010) A novel hydrazine electrochemical sensor based on the high specific surface area graphene. Microchim Acta 169:1–6.

[50] Peng H, Liang C (2016) Electrochemical determination of hydrazine based on polydopamine-reduced graphene oxide nanocomposite. Fullerenes, Nanotub. Carbon Nanostructures